Applied Materials Today 44 (2025) 102714

Contents lists available at ScienceDirect

Applied Materials Today

journal homepage: www.elsevier.com/locate/apmt

# $Yb^{3+}$-Mediated Luminescence Enhancement in $Er^{3+}$-Doped 3D-Printed $ZrO_2$ Microarchitectures

Cristian Rosero-Arias [a,b,*], Geraldo Cristian Vásquez [c,*], Manuel Herrera-Zaldívar [d], R. Margoth Córdova-Castro [e], Israel De Leon [f,g], Francisco Ruiz-Zepeda [h,i], Han Gardeniers [a], David Maestre [c], Alan Aguirre-Soto [b,*], Arturo Susarrey-Arce [a,*]

[a] Department of Chemical Engineering, Mesoscale Chemical Systems, MESA+ Institute, University of Twente, PO Box 217, Enschede, 7500 AE, The Netherlands
[b] School of Engineering and Sciences, Tecnológico de Monterrey, Eugenio Garza Sada 2501, Monterrey 64849, NL, Mexico
[c] Departamento de Física de Materiales, Facultad de Ciencias Físicas, Universidad Complutense de Madrid, 28040, Madrid, Spain
[d] Centro de Nanociencias y Nanotecnología, Universidad Nacional Autónoma de México, Km 107 Carretera Tijuana-Ensenada, Ensenada, Baja California, C.P. 22800, México
[e] Department of Physics, University of Ottawa, Ottawa, Ontario, K1N 6N5 Canada
[f] School of Electrical Engineering and Computer Science, University of Ottawa, Ottawa, K1N 6N5 Canada
[g] ASML Netherlands B.V., De Run 6501, 5504 DR Veldhoven, The Netherlands
[h] Department of Materials Chemistry, National Institute of Chemistry, Hajdrihova 19, Ljubljana, SI-1000 Slovenia
[i] Department of Physics and Chemistry of Materials, Institute of Metals and Technology, Lepi pot 11, Ljubljana, Slovenia

ARTICLE INFO

*Keywords:*
Additive Manufacturing
Ceramics
Rare-Earth
$ZrO_2$
Co-doping

ABSTRACT

Lanthanide-doped $ZrO_2$ ceramics are promising materials for optics due to their high refractive index and tunable luminescent properties. In this study, we investigated the impact of $Yb^{3+}$ and $Er^{3+}$ dopant concentrations on the emission behavior of lanthanide-doped 3D $ZrO_2$ microarchitectures fabricated using two-photon lithography. Thermal treatments have been carried out at 600°C and 750°C to promote the stabilization of the $ZrO_2$ tetragonal phase (*t*-$ZrO_2$) and at 1000°C to induce phase transition in $ZrO_2$ to the monoclinic (*m*-$ZrO_2$) phase in the 3D microarchitectures. Scanning transmission electron microscopy confirmed the crystallinity changes across the thermal treatments. Photoluminescence (PL) and cathodoluminescence (CL) measurements confirm emission bands of $Yb^{3+}$ and $Er^{3+}$ single dopants and $Yb^{3+}$:$Er^{3+}$ co-dopants. Variations in $Yb^{3+}$ content reveal that the PL emission of $Er^{3+}$ increases (e.g., $^4S_{3/2} \rightarrow {}^4I_{15/2}$), which is attributed to the interplay between the dopant concentrations, defect structures and the $ZrO_2$ host. The results highlight the importance of $ZrO_2$ microarchitectures' crystallinity and co-doping relationship, which enable the promotion of $Er^{3+}$ emissions. We expect our research will find applications in 3D optical systems.

## 1. Introduction

The sharp, characteristic emissions of trivalent lanthanide ions ($Ln^{3+}$) have long attracted attention due to their applications in advanced optical technologies. Unlike other emitters, $Ln^{3+}$ ions exhibit narrow-band emissions originating from shielded 4f–4f electronic transitions [1,2]. These emissions, covering visible to near-infrared regions, make $Ln^{3+}$ ions indispensable in lasers, optical amplifiers, displays, and sensors [3,4]. However, their luminescent properties are not solely intrinsic to $Ln^{3+}$ ions. $Ln^{3+}$ requires a host material, which plays a decisive role in determining spectral properties and energy transfer (ET) dynamics [5,6]. Among host materials, zirconium dioxide ($ZrO_2$) stands out for its wide band gap (4-4.5 eV), broad transparency range (spanning from ultraviolet to mid-infrared), and low phonon energy (~470 $cm^{-1}$) [7]. $ZrO_2$ exists in multiple crystallographic phases, such as monoclinic (*m*-$ZrO_2$) and tetragonal (*t*-$ZrO_2$), with characteristic luminescence mainly originated by defects [8]. At room temperature and ambient pressure, the monoclinic phase is the most stable, while the tetragonal phase can be stabilized through doping with aliovalent ions or by reducing crystallite size below ~30 nm to lower surface energy [9]. In $ZrO_2$, crystal defects often arise from synthetic methods [10], as synthetic methods often lack control over perfect crystal growth formation

* Corresponding authors.
*E-mail addresses:* c.roseroarias@utwente.nl (C. Rosero-Arias), gc.vasquez@ucm.es (G.C. Vásquez), alan.aguirre@tec.mx (A. Aguirre-Soto), a.susarreyarce@utwente.nl (A. Susarrey-Arce).

https://doi.org/10.1016/j.apmt.2025.102714
Received 30 January 2025; Received in revised form 12 March 2025; Accepted 4 April 2025
Available online 13 April 2025

and thermodynamics [11]. Although the number and defect type can be modulated through various conditions in the $ZrO_2$ host (e.g., chemical environment during annealing or doping), such defects can act as traps for charge carriers, leading to non-radiative recombination or back ET in $Ln^{3+}$ doped $ZrO_2$ systems [12]. Reducing defects is a strategy to minimize non-radiative losses, enabling, for example, $Ln^{3+}$ sharp luminescence lines [13].

While traditional methods like solid-state reactions and sol-gel techniques are effective for bulk materials, they lack the precision to produce doped 3D arbitrary complex designs [14–16]. Recently, we reported suboptimal doping to limit $Ln^{3+}$ emission in co-doped systems with 3D complex designs made by two-photon lithography and subsequent annealing steps [17]. In the case of $Yb^{3+}$ and $Er^{3+}$ co-dopants, $Yb^{3+}$ can act as a sensitizer, transferring energy to $Er^{3+}$, enabling visible emissions of value in lasers and energy transfer devices [18]. Nevertheless, understanding the co-doping emissions within a micrometric host matrix remains challenging for 3D microarchitectures, as it calls for complex custom-made specialized optical techniques. However, instead of specialized techniques, CL and PL spectroscopy are relatively accessible techniques that can help to understand optical behavior in $Ln^{3+}$-doped microarchitectures. Hence, they were selected in this study to evaluate $Yb^{3+}$ and $Er^{3+}$ emissions in inorganic $ZrO_2$ microarchitectures.

The 3D $ZrO_2$ microarchitectures can be fabricated at the highest definition using additive manufacturing (AM), also known as 3D printing. AM methods include two-photon lithography (TPL), which provides tenths of nanometer control over micrometer-size luminescent microarchitecture features [11,19,20]. TPL uses focused femtosecond laser pulses, triggering localized photopolymerization within a photoresin containing inorganic salts and photoinitiator, allowing tenth-of-nanometer voxel-level control over features in intricate pre-ceramic architectures (i.e., metal-organic printed microarchitectures) [21]. The adaptability of photoresin composition in TPL is essential to achieving glass and ceramics with tailored optical properties, enabling applications in photonics, micro-optics, and functional microdevices [22].

Once the pre-ceramic microarchitecture has been achieved, the thermal annealing removes the organic components of the pre-ceramic microarchitecture, forming a ceramic replica. During this process, the crystalline phase is stabilized. Alkali-earth perovskites are an example of phase-stabilized complex oxides fabricated with TPL [19]. For less complex oxide systems like $ZrO_2$ systems, annealing temperatures can lead to either the *t*-$ZrO_2$ (600–750°C) or the *m*-$ZrO_2$ (above 750°C) [23]. Independently from the crystal phase, the host crystallinity is another key parameter. The crystallite environment is expected to vary depending on the precursor for printing. This is the case for 3D $ZrO_2$ [17, 24], where variations in $ZrO_2$ crystallographic phases and crystallite size can be obtained depending on the Zr precursors utilized.

In the $Ln^{3+}$ doped $ZrO_2$ systems, $Yb^{3+}$and $Er^{3+}$ ions are well-suited for the $ZrO_2$-host. Unlike silica-based hosts, an additional advantage of crystalline $ZrO_2$ is that it provides a robust environment that supports $Ln^{3+}$ distribution while reducing clustering and associated quenching pathways [25–27]. Within the host, $Yb^{3+}$ can emit near-infrared light around 975 nm, corresponding to the $^2F_{5/2}$–$^2F_{7/2}$ transition [28]. $Er^{3+}$, on the other hand, exhibits characteristic visible emissions in the green range $^4S_{3/2}$–$^4I_{7/2}$ and red range ($^4F_{9/2}$–$^4I_{15/2}$) alongside near-infrared features [28]. Combining these dopants within the $ZrO_2$ host allows one to explore their dependency emission behavior. A way forward for understanding light emission based on the use of PL and CL to characterize the luminescence of $Yb^{3+}$, $Er^{3+}$, and under different co-doping concentrations. PL, with a 325 nm excitation source, offers detailed insights into processes close to the $ZrO_2$ interface [29], while CL, equipped with electron beam excitation, primarily probes luminescence from the bulk [30]. PL and CL techniques can also excite diverse luminescent mechanisms, providing complementary information for assessing the $Yb^{3+}$ and $Er^{3+}$ emissions. Therefore, we can determine the $Yb^{3+}$ and $Er^{3+}$ emissions and their contributions by comparing the results from the PL and CL techniques.

This work presents an approach to fabricating $Ln^{3+}$-doped $ZrO_2$ microarchitectures using a Zr-methacrylate-based photoresin optimized for TPL. We explore the impact of thermal cycling by evaluating the effects of three-step thermal annealing (600°C, 750°C, and 1000°C). The effect of each thermal annealing on the crystallinity and its impact during phase transitions of 3D-printed $ZrO_2$ microarchitectures is discussed. The results are supported by structural and chemical characterization (i.e., SEM-EDX and STEM-EDX). The effect of the $Ln^{3+}$ concentration has also been investigated, as well as the co-doping-related effects. The fabricated microarchitectures' dopant levels are adjusted from single dopants ($Yb^{3+}$ and $Er^{3+}$) to 2.5 mol% and 0.35 mol %. For co-doped photoresins, the $Yb^{3+}$:$Er^{3+}$ molar ratios are: 7:1 (2.5 mol% Yb, 0.35 mol% Er), 2:1 (1.25 mol% Yb, 0.66 mol% Er), 1:2 (0.66 mol% Yb, 1.25 mol% Er). 1:7 (0.35 mol% Yb, 2.5 mol% Er). The luminescent properties of the fabricated microarchitectures are then assessed with CL and PL. The results highlight that $Yb^{3+}$ can mediate luminescence enhancement in $Er^{3+}$-doped 3D-printed $ZrO_2$ microarchitectures, paving the path for the fabrication of light emission elements.

## 2. Results and Discussion

### 2.1. Manufacturing of $Ln^{3+}$-doped $ZrO_2$ microarchitectures

To fabricate the $Yb^{3+}$, $Er^{3+}$ doped, and $Yb^{3+}$:$Er^{3+}$ co-doped $ZrO_2$ microarchitectures, a TPL-compatible photoresist was developed. This formulation builds upon previous work to overcome challenges related to resin composition, dopant integration, and phase stability during thermal processing [17]. The resin preparation, printing, and subsequent thermal treatments are outlined in Fig. 1. The resin preparation begins with the dissolution of zirconium methacrylate (ZrM) in acetic acid (AcA), N,N-dimethylacetamide (DMAc), and dichloromethane (DCM). These solvents have been chosen for their polar characteristics, which aid in dissolving ZrM and resolving solubility challenges inherent to Zr-based precursors. A multifunctional crosslinking agent, pentaerythritol triacrylate (PETA), is also added to the photoresin to enhance the mechanical and structural stability of the printed microarchitectures. The photoresin includes a photoinitiator, 7-diethylamino-3-thenoylcoumarin (DETC), tailored for TPL. Lanthanide salts ($Yb^{3+}$ and $Er^{3+}$ dopants) are then introduced in varying concentrations. Dopant levels are adjusted to avoid resin saturation. Single-doped photoresins are prepared at 2.5 mol% and 0.35 mol% for $Yb^{3+}$ and $Er^{3+}$, relative to Zr. For co-doped photoresins, the $Yb^{3+}$:$Er^{3+}$ molar ratios and the following concentrations are chosen: 7:1 (2.5 mol% Yb, 0.35 mol% Er), 2:1 (1.25 mol% Yb, 0.66 mol% Er), 1:2 (0.66 mol% Yb, 1.25 mol% Er). 1:7 (0.35 mol% Yb, 2.5 mol% Er). Each dopant mixture is dissolved uniformly in the zirconium-rich photoresin.

The formulated resins are then used for the TPL fabrication of buckyball and octet-truss microarchitectures, as illustrated in Fig. 1**a**. During the TPL printing step, the photoresin is drop-casted onto a 9 × 9 mm silicon substrate and covered with a glass slide separated by polyimide spacers. The printed microarchitectures (e.g., pre-ceramic buckyballs and octet-truss lattices) composed of metal-organic components are then developed in methanol and isopropanol (IPA) to remove uncured resin. These pre-ceramic structures act as templates for thermal annealing steps, as detailed in the "Experimental Methods" section, which dictates the final phase and morphology of the ceramic replicas.

Thermal annealing is carried out in three cycles in ambient air at 1 atm. In the first cycle (600°C), organic components are removed, resulting in the formation of a microarchitecture (Fig. 1**b.I-1b.II**) that is primarily composed of *t*-$ZrO_2$. This step also induces isotropic shrinkage of approximately 80% from the pre-ceramic to the ceramic microarchitecture (**Figure S1a**); the microarchitecture reduces its dimensions from ~40 μm to ~9 μm while preserving its characteristic morphology (i.e., buckyball or octet-truss). **Figure S1a** and **Figure S1b** show a beam

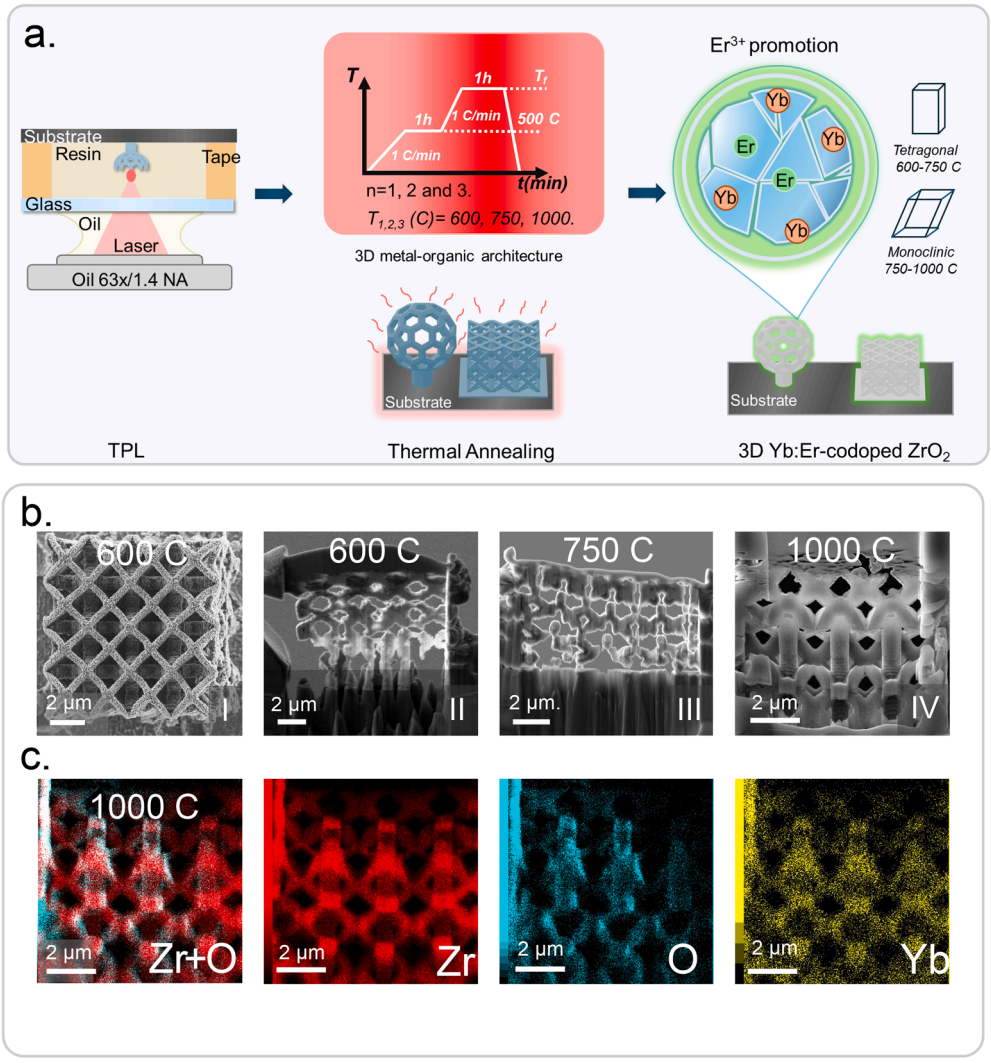


**Fig. 1.** a) Manufacturing process: TPL 3D printing using a custom-made photoresin in an oil immersion objective. The metal-organic microarchitecture is exposed to thermal annealing in air and shrinks into the final $Ln^{3+}$-doped $ZrO_2$ replica. b.I) SEM images of 2.5 mol% Yb $^{3+}$-doped $ZrO_2$ octet-truss treated at 600°C and SEM image of a FIB prepared specimen. In this case, b.II) is after Cycle 1 (600°C), b.III) after Cycle 2 (750°C), and b.IV)after Cycle 3 (1000°C). c) STEM-EDX merged Zr+O, and a single elemental map for Zr, O, and Yb is displayed for the thermally treated microarchitecture at 1000 °C.

size comparison between the metal-organic microarchitecture and the reduced replica. SEM images of **Figure S1** of the fabricated microarchitectures confirm that the primary shrinkage occurs mainly during the first annealing step. In the second cycle (750°C, Fig. 1**b.III**), there is no shrinkage, as evidenced by the beam diameter in **Figure S1b** and **Figure S1c**, estimated close to 0.834 µm and 0.796 µm, respectively. Similar to Fig. 1**b.III**, the third cycle at 1000°C (Fig. 1**b.IV**) does not reveal additional shrinkage with a beam diameter close to 0.833 µm (**Figure S1d**). It is essential to note that the same annealing in Fig. 1**b.I-IV** has been applied to all single dopant concentrations and co-dopant combinations.

To further investigate the phase composition and microstructure of the annealed architectures, SEM and scanning transmission electron microscopy (STEM) are employed. SEM-Energy-dispersive X-ray spectroscopy (EDX) confirms the chemical composition after the final annealing step at 1000°C (Fig. 1**c**). The merged elemental map (Fig. 1**c**) reveals the distribution of Zr and O, indicating the successful formation of the $ZrO_2$ framework. The detection of Yb signals further corroborates the dopant incorporation. It is worth remarking that no changes are expected for Er-doped and co-doped microarchitectures. Hence, the results shown here are representative of this system.

The representative microarchitecture doped with 2.5 mol% Yb is further analyzed. STEM is employed (Fig. 2) to further analyze the effects of thermal annealing on the structural evolution of Yb-doped $ZrO_2$ microarchitectures annealed at 600°C, 750°C, and 1000°C (Fig. 1**b**). From our previous results [17], *t*-$ZrO_2$ is formed at the temperatures 600°C and 750°C, with averaged crystal size around ~6 nm and ~10 nm, respectively. At 600°C (Cycle 1, Fig. 1**b.II**), TEM images (Fig. 2**a**) show that the microarchitecture comprises small crystallites. Although Fig. 1**b.I** and Fig. 2**a** confirm the presence of crystalline domains; the possibility of amorphous regions within the Yb-doped $ZrO_2$ microarchitecture remains. High-magnification STEM shows $ZrO_2$ lattice fringes corresponding to a spacing of 0.29 nm, consistent with the (101) planes of *t*-$ZrO_2$ [31], as demonstrated by the fast Fourier transform (FFT) analysis in Fig. 2**c**. In addition, FFT analysis shows (101), (112), and (211) planes of *t*-$ZrO_2$ (JCPDS cards no. 17-0923). These observations align with x-ray diffraction (XRD) patterns of Ln-doped $ZrO_2$ powders (**Figure S2a**), indicating the *t*-$ZrO_2$ phase dominance at this annealing temperature.

Our attributions on the small crystallites and possibly amorphism [31–33] at 600°C (Cycle 1, Fig. 1**b.II**) are further supported by re-annealing the Yb-doped $ZrO_2$ microarchitecture at 750°C (Cycle 2, Fig. 1**b.III**). STEM image in Fig. 2**d** demonstrates an increase in the crystallite content, as indicated by sharper and more well-defined lattice

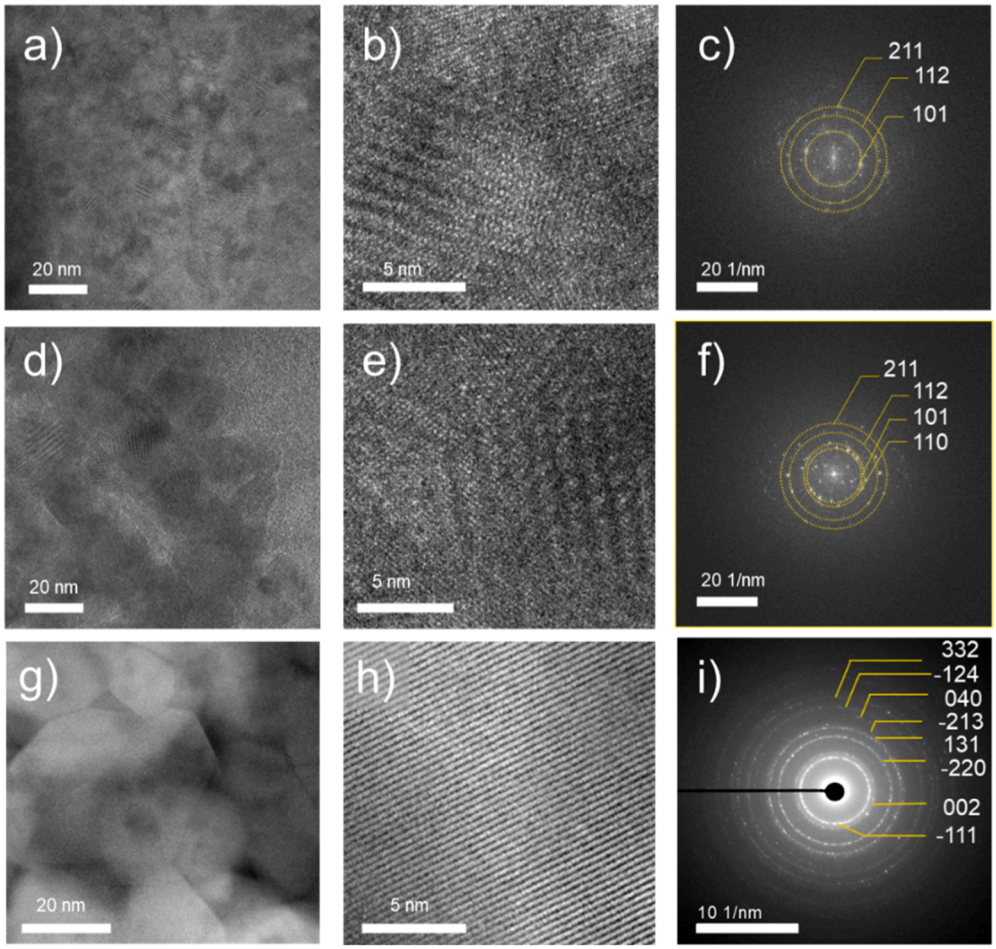


**Fig. 2.** STEM of an 2.5 mol% Yb-doped octet-truss annealed at 600°C (a), 750°C (d), and 1000°C (g), corresponding to the FIB specimen shown in Fig. 1. .High-magnification STEM images for octet-truss annealed at 600°C (b), 750°C (e) and 1000°C (h). Corresponding FFT is shown in (c, f), and experimental diffraction pattern in (i).

fringes in Fig. 2**d-e**. In addition to the predominant planes observed at 600°C (i.e., (101), (112), and (211)), the FFT pattern for Cycle 2 (Fig. 2**f**) includes the appearance of the (110) *t*-$ZrO_2$ plane, further confirming crystallinity changes in the microarchitectures. These observations are consistent with previous findings in similar *t*-$ZrO_2$ systems [17,34,35]. We then analyze the Yb-doped $ZrO_2$ microarchitecture annealed at 1000°C (Cycle 3, Fig. 1**b.IV**) in Fig. 2**g**-2**i**. STEM images reveal significant changes in the microarchitecture with relatively well-defined lattice fringes (Fig. 2**g**). High-magnification STEM-ADF (Fig. 2**h**) displays a well-defined crystal lattice, and the experimental diffraction pattern (Fig. 2**i**) shows crystal planes (-111), (002), (-220), (131), (-213), (040), (-124) and (332) ascribed to *m*-$ZrO_2$ (JCPDS card no. 37-1484) [36]. These findings align with XRD data for powders annealed at 1000°C (**Figure S2c**), which indicates phase transition from *t*- to *m*-$ZrO_2$. In addition, we should not disregard the possibility of *t*-$ZrO_2$ in **Figure S2c**, as our results indicate an incomplete *m*-$ZrO_2$ transformation.

In short, we selected representative $Yb^{3+}$-doped microarchitectures doped at 2.5 mol%. Figs. 1 and 2 illustrate the morphological characteristics and evolution of $Yb^{3+}$-doped $ZrO_2$ microarchitectures, transitioning from small crystallites at 600°C to large crystallites at 750°C and even larger crystallites along with *t*-to-*m* phase transformation at 1000°C. The optical results are presented in the following sections.

### 2.2. Luminescence of single $Yb^{3+}$-and $Er^{3+}$-doped $ZrO_2$ microarchitectures

Next, we carried out CL and PL measurements of the produced microarchitectures. In this case, CL, a high-energy electron beam with a penetration depth of ~1-2 μm [37], probes the bulk of the microarchitecture and excites a broader range of energy states, compared to UV light source from PL, which is limited to ~100 nm [8]. These complementary techniques provide insights into the dopant emission across fabricated microarchitectures.

#### 2.2.1. CL of single $Yb^{3+}$-and $Er^{3+}$-doped $ZrO_2$ microarchitectures

The CL spectra of single-doped $ZrO_2$ microarchitectures (Fig. 3**a-c**, left panels) provide insight into the luminescence behavior of $Yb^{3+}$ and $Er^{3+}$ under three thermal treatment cycles (Fig. 1). Four single-doped microarchitectures are analyzed: $Yb^{3+}$ at 2.5 mol% and 0.35 mol%, and $Er^{3+}$ at 2.5 mol% and 0.35 mol%. These configurations allow us to investigate the effects of varying dopant concentrations, with 2.5 mol% representing a high concentration and 0.35 mol% a low concentration. Specifically, the evolution of $Yb^{3+}$ and $Er^{3+}$ emissions across the three consecutive thermal treatments in the $ZrO_2$ microarchitectures is evident.

In the $Yb^{3+}$ single-doped microarchitectures ($Yb^{3+}$ at 2.5 mol% and 0.35 mol%, in Fig. 3**a**-3**c**), no characteristic peaks corresponding to the $^2F_{5/2} \rightarrow {}^2F_{7/2}$ transition of $Yb^{3+}$ are observed in the CL spectra due to the limitations of the CL detector for capturing near-infrared (NIR) emissions. Instead, the spectra are dominated by broad defect-related luminescence originating from the $ZrO_2$ matrix. Defect-related emissions are broad and most pronounced in Cycle 1 (600°C, Fig. 3**a**). For the other cycles, the defects CL emission remains similar, as seen in Fig. 3**b** (Cycle 2, 750°C) and Fig. 3**c** (Cycle 3, 1000°C). **Figures S3a-b** show an

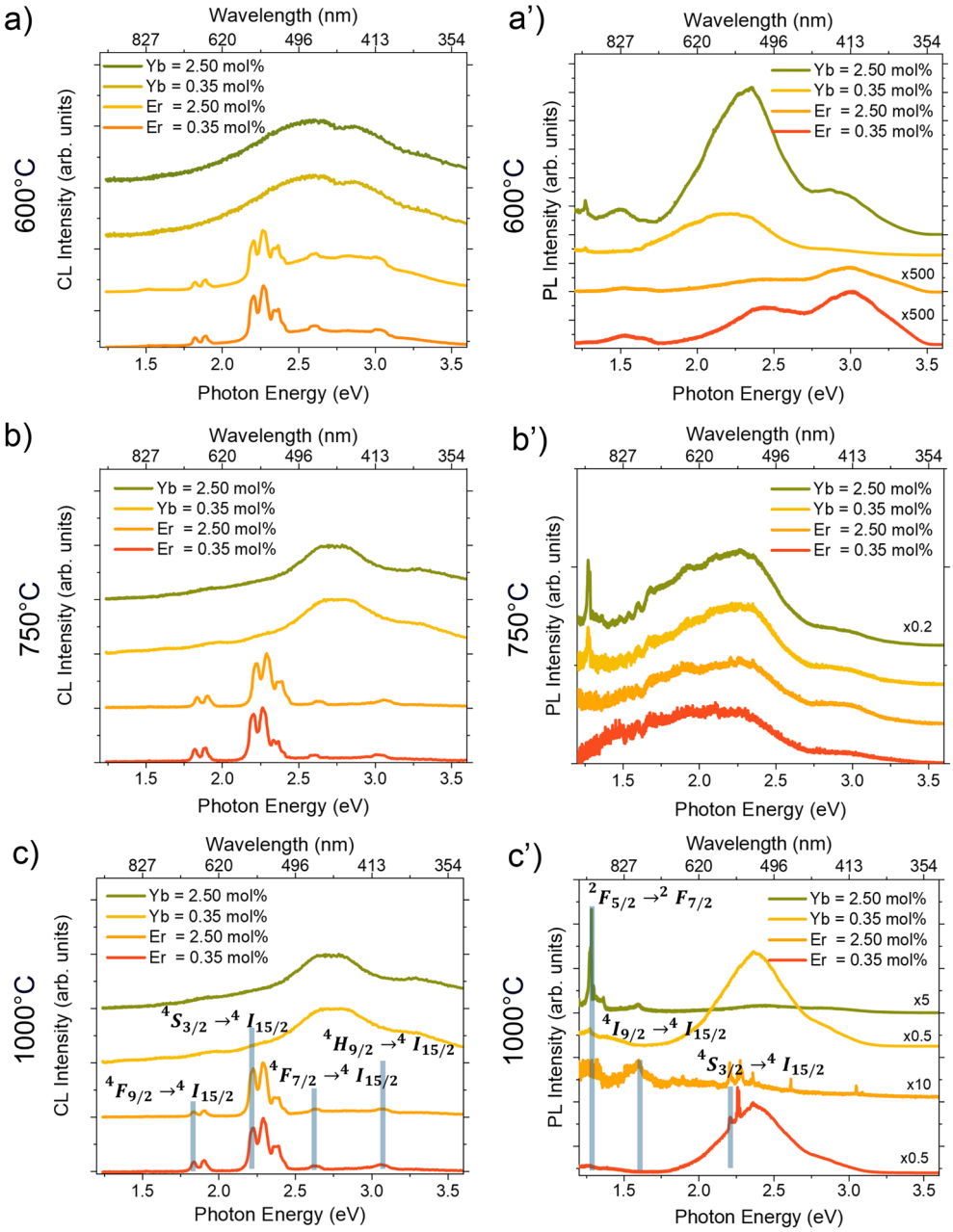


**Fig. 3.** CL and PL spectra of $Yb^{3+}$ and $Er^{3+}$ single doped $ZrO_2$ microarchitectures for the three thermal cycles. Each row corresponds to a thermal treatment cycle: (a, a') Cycle 1 at 600°C, (b, b') Cycle 2 at 750°C, and (c, c') Cycle 3 at 1000°C, all in 1 atm atmosphere. The left panels (a, b, c) present CL measurements, while the right panels (a', b', c') depict PL measurements at an excitation wavelength of 325 nm. The results for $Yb^{3+}$ 2.5 mol% (green), $Yb^{3+}$ 0.35 mol% (yellow), $Er^{3+}$ 2.5 mol% (orange), and $Er^{3+}$ 0.35 mol% (red) show the influence of dopant concentration.

assessment of the defect where the Gaussian deconvolution of the defects accompanies this assessment. The defects emissions are attributed to oxygen vacancies (1.61 eV), lattice strain (2.59 eV and 3.29 eV), and carbon impurities (2.92 eV), respectively [38,39].

For $Er^{3+}$ single-doped microarchitectures, the CL spectra exhibit significant differences across the various annealing cycles (Fig. 3**a-c**). Characteristic $Er^{3+}$ transitions $^4F_{9/2} \rightarrow {}^4I_{15/2}$ (i.e., red emission) and $^4S_{3/2} \rightarrow {}^4I_{15/2}$ (i.e., green emission) are observed in the single-doped material, as shown in Fig. 3. In Cycle 1 (600°C, Fig. 3**a**), the $Er^{3+}$ single-doped microarchitectures show a broad contribution from defects (i.e., 2 – 3.5 eV). For Cycle 2 (750°C, Fig. 3**b**), the $Er^{3+}$ single-doped microarchitectures present spectra with a lower defect influence due to the absence of the broad defect band in Fig. 3**a**. This behavior is likely due to the increased crystallinity of the *t*-$ZrO_2$ shown in STEM images in Fig. 2. Similar results to those of Cycle 2 are observed for Cycle 3 (1000°C, Fig. 3**c**). The results reveal an emission with low defect contributions at 2.64 eV (469 nm, $^4F_{7/2} \rightarrow {}^4I_{15/2}$) and 3.06 eV (405 nm, $^2H_{9/2} \rightarrow {}^4I_{15/2}$). The emergent emissions in cycles 2 and 3 can be related to the increase in crystallinity (Fig. 2). No significant spectral variations associated with the *t*-$ZrO_2$ to *m*-$ZrO_2$ phase transformation are observed in the microarchitectures. A summary of the $Ln^{3+}$ emissions is presented in **Table S1** [40–46].

### *2.2.2. Photoluminescence of single $Yb^{3+}$-and $Er^{3+}$-doped $ZrO_2$ microarchitectures*

The PL spectra of single-doped $ZrO_2$ microarchitectures, shown in Fig. 3**a'-c'**, provide valuable insights into the luminescence behavior of $Yb^{3+}$ and $Er^{3+}$ under UV excitation (325 nm) across the three thermal

treatment cycles (Fig. 1). We observed a larger variation in PL spectra compared to CL results (Section 2.2.1), which aligns with the lower excitation energy and shallower penetration depth of UV light (~100 nm) in PL. In contrast, CL, with its higher energy electron beam (~1-2 μm penetration depth), excites a broader range of states, leading to more uniform spectral features across samples. In Cycle 1 (600°C, Fig. 3**a'**), the PL spectra reveal small peaks corresponding to the $^2F_{5/2} \rightarrow {}^2F_{7/2}$ transition of $Yb^{3+}$ (~1.27 eV, 975 nm). No $Er^{3+}$ emissions are observed in single-doped microarchitectures in Fig. 3**a'**. Broad emission regions (~1.7-3.5 eV) can be attributed to defects. The results indicate that at 600°C, various defect types are present within the crystallites. Our attribution is confirmed by the differences in emission intensities observed across the diverse microarchitectures in Fig. 3**a'**. Although intensity differences are observed in Fig. 3**a'**, the overall broad PL peak remains with similar components. This is confirmed by the Gaussian fitting of the $Yb^{3+}$ single-doped microarchitecture, whose PL spectrum is shown in **Figure S4**. In **Figure S4**, we identify four defect contributions: PL I at 1.49 eV, PL II at 2.14 eV (related to $F_{AA+}$ centers), PL III at 2.39 eV (correlated with $Zr^{3+}$ states), and PL IV at 2.92 eV (associated with interstitial carbon) [38,39]. Interestingly, emissions related to oxygen vacancies are not identified as in CL measurements. This could suggest that the contribution of oxygen vacancies is mainly from the bulk of the microarchitecture. In Cycle 2 (750°C, Fig. 3**b'**), the contribution related to interstitial carbons is reduced compared to in Fig. 3**a'**. The broad-emission spectra in Fig. 3**b'** show regions with similar defect contributions across all single-doped microarchitectures.

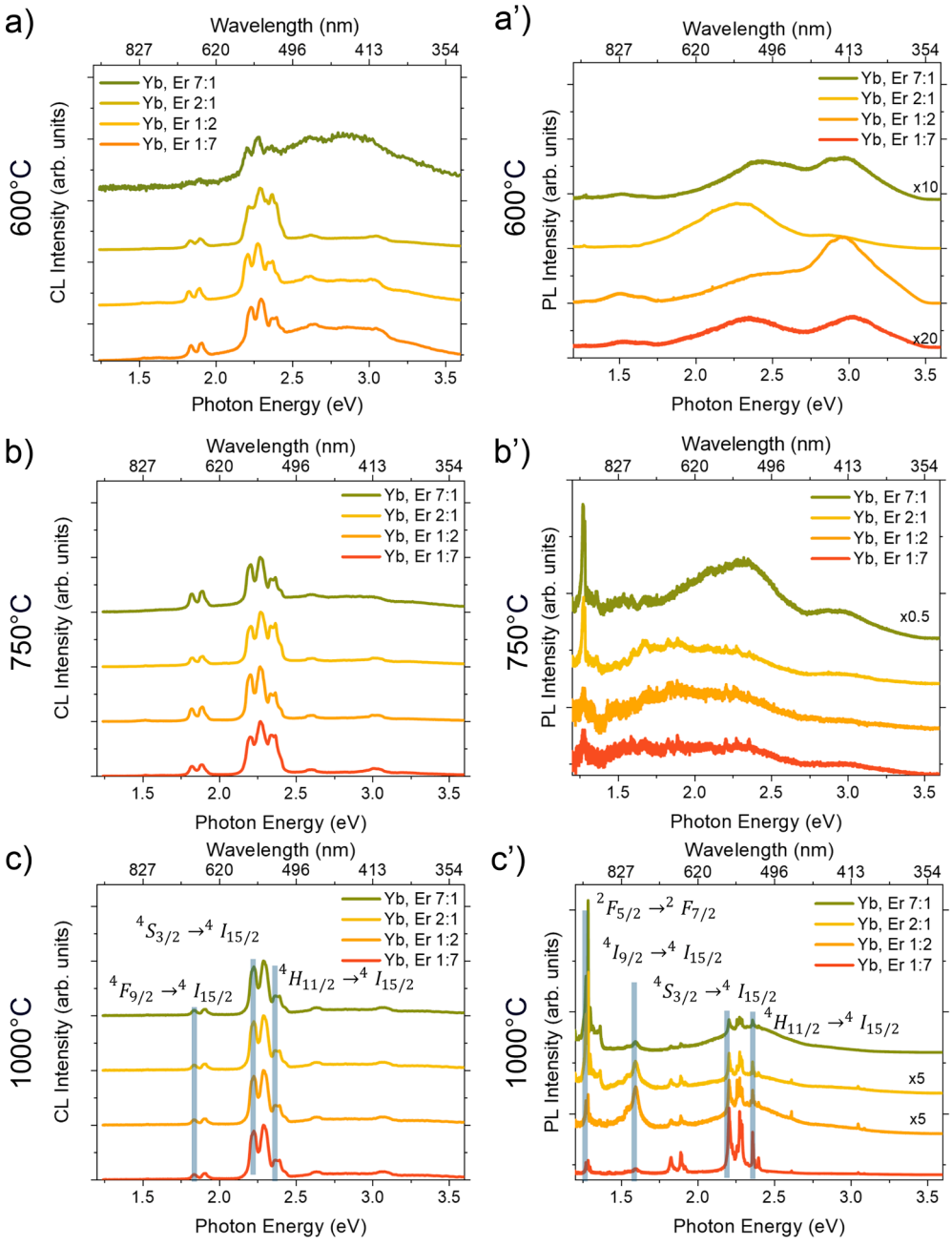


**Fig. 4.** CL and PL spectra of $Yb^{3+}$:$Er^{3+}$-doped $ZrO_2$ microarchitectures under three thermal treatment cycles. The left panels (a, b, c) represent CL measurements, while the right panels (a', b', c') depict PL measurements at an excitation wavelength of 325 nm. Each row corresponds to a thermal treatment cycle: (a, a') Cycle 1 at 600°C, (b, b') Cycle 2 at 750°C, and (c, c') Cycle 3 at 1000°C, all in 1 atm air ambient. The results for different $Yb^{3+}$:$Er^{3+}$ doping ratios—7:1 (green), 2:1 (yellow), 1:2 (orange), and 1:7 (red)—are plotted to highlight the influence of dopant concentration on luminescence behavior.

In Cycle 3 (1000°C, Fig. 3**c'**), the *m*-$ZrO_2$ becomes predominant, as found in XRD and STEM (**Figure S2c** and Fig. 2**i**). This microarchitecture leads to peaks corresponding to the $^2F_{5/2} \rightarrow {}^2F_{7/2}$ transition of $Yb^{3+}$ at 975 nm and the $^4S_{3/2} \rightarrow {}^4I_{15/2}$ green emission of $Er^{3+}$ in their respective single-doped microarchitectures. In Fig. 3**c'**, the Yb emission peak at 2.5 mol% has a sharper intensity compared to previous defect contributions from Cycles 2 and 3. However, at a small $Yb^{3+}$ concentration (0.35 mol %), the defect band (2.0-3.0 eV) related to *m*-$ZrO_2$ is predominant, indicating that higher $Yb^{3+}$ concentrations are required to compensate for defect contributions in printed microarchitectures. For Er-doped microarchitectures, the ones with 2.5 mol% concentration present characteristic $Er^{3+}$ emissions, including a weak infrared contribution ($^4I_{9/2} \rightarrow {}^4I_{15/2}$). Notably, defect-related contributions in $Er^{3+}$ (2.5 mol%) microarchitectures are reduced following the thermal treatment at 1000°C. Such behavior is not observed at 0.35 mol% (Fig. 3**c'**), where a broad defect emission band is presented between 1.7-3.2 eV, overlapping with the $^4S_{3/2} \rightarrow {}^4I_{15/2}$ transition (**Table S1**). It is, therefore, safe to say that in both 0.35 mol% $Yb^{3+}$ and $Er^{3+}$-doped microarchitectures, the defect emission band is dominant compared to the respective $Ln^{3+}$ transitions.

In summary, the CL and PL spectra of single-doped $Yb^{3+}$- and $Er^{3+}$-doped $ZrO_2$ microarchitectures highlight distinct luminescence behaviors and defect contributions across thermal cycles. CL reveals the dominance of $ZrO_2$ matrix defects in Cycle 1 (600°C), with reduced defect emissions and enhanced crystallinity evident in Cycle 2 (750°C) and Cycle 3 (1000°C), which has a phase transformation to *m*-$ZrO_2$. In both cases, sharper characteristic emissions, particularly the $Yb^{3+}$ ($^2F_{5/2} \rightarrow {}^2F_{7/2}$) transition and $Er^{3+}$ ($^4S_{3/2} \rightarrow {}^4I1_{5/2}$) green emission have been found. PL further confirms these trends, with defect-related emissions decreasing as the $Ln^{3+}$ increases and the annealing progresses, emphasizing the interplay between thermal treatment, dopant concentration, and crystallinity.

### 2.3. $Yb^{3+}$:$Er^{3+}$ co-doped $ZrO_2$ microarchitectures

#### 2.3.1. CL of $Yb^{3+}$:$Er^{3+}$ co-doped $ZrO_2$ microarchitectures

In the CL spectra (Fig. 4**a-c**), characteristic peaks from $Er^{3+}$ are identified (**Table S1**), including emissions in the green region corresponding to the $^4S_{3/2} \rightarrow {}^4I_{15/2}$ transition (2.26 eV) and $^2H_{11/2} \rightarrow {}^4I_{15/2}$ (2.36 eV) transitions and weaker contributions in the red region associated with $^4F_{9/2} \rightarrow {}^2I_{15/2}$ transitions [45,44]. Additionally, emissions from $ZrO_2$ defects appear as a broad emission band in the 1.2–4.0 eV region (**Figure S3a**). Notably, the CL detector used in this study is blind to near-infrared (NIR) emissions, precluding the direct observation of $Yb^{3+}$ emissions, such as the $^2F_{5/2} \rightarrow {}^2F_{7/2}$ transition expected at 975 nm [43]. The results show a pronounced defect-related luminescence, particularly in Cycle 1 (600°C, Fig. 4**a**), where amorphous regions and incomplete crystallization are observed in STEM measurements (Fig. 2). The relative intensity of defect emissions in Fig. 4**a** is notably higher for microarchitectures with $Yb^{3+}$:$Er^{3+}$ molar ratios of 7:1 and 1:7, corresponding to the highest total dopant concentrations. Conversely, ratios of 2:1 and 1:2 exhibit reduced defect emissions. After thermal treatment at 750°C (Cycle 2, Fig. 4**b**) and 1000°C (Cycle 3, Fig. 4**c**), minor changes in the emissions profiles are observed and the defect-related emissions decrease for all doping ratios, suggesting a reduction of the defects and amorphous regions in the microarchitecture.

#### 2.3.2. Photoluminescence of $Yb^{3+}$:$Er^{3+}$ co-doped $ZrO_2$ microarchitectures

The PL spectra from cycle 1 (Fig. 4**a'**, right panels) reveal emissions similar to those in Fig. 3, which are attributed to defects in the $ZrO_2$ microarchitectures. However, the PL spectra (Fig. 4**b'-c'**, right panels) reveal emissions from $Er^{3+}$ and $Yb^{3+}$ under UV excitation (325 nm), which provides sufficient energy to populate the $^2F_{5/2}$ state of $Yb^{3+}$. The excitation of the host matrix likely leads to multiple cross-relaxation (CR) and ET processes, where defects in *t*-$ZrO_2$ and *m*-$ZrO_2$ influence the luminescence dynamics. $Yb^{3+}$ emissions, centered around 975 nm ($^2F_{5/2} \rightarrow {}^2F_{7/2}$), are observed alongside $Er^{3+}$ green ($^4S_{3/2} \rightarrow {}^4I_{15/2}$) and red ($^4F_{9/2} \rightarrow {}^4I_{15/2}$) emissions. The relative intensity of $Yb^{3+}$ emissions increases with higher $Yb^{3+}$ concentrations. For Cycle 2 (750°C, Fig. 4**b'**), $Yb^{3+}$ emissions at 975 nm become apparent, accompanied by more consistent defect emissions across microarchitectures, indicating that Cycle 1 generally leads to a vast number of defects overshadowing $Ln^{3+}$ emissions. Improved crystallinity in Fig. 4**b'** likely contributes to the increased $Yb^{3+}$ emission. At the 7:1 ratio, $Yb^{3+}$ and defect emissions are strongest, while at the 1:7 ratio, $Yb^{3+}$ emissions are weaker. No evident emission from $Er^{3+}$ is observed in the assessed PL region. However, in Cycle 3 (1000°C, Fig. 4**c'**), the crystallinity in our microarchitectures increases further, sharpening $Yb^{3+}$ emissions, with the pronounced peak observed at the 7:1 ratio. Similarly, $Er^{3+}$ emissions ($^4S_{3/2} \rightarrow {}^4I_{15/2}$) are strongest at the 1:7 ratio, demonstrating a complementary effect between $Yb^{3+}$ and higher $Er^{3+}$ concentrations increasing green luminescence (~2–2.5 eV). Infrared emissions from $Er^{3+}$ ($^4I_{9/2} \rightarrow {}^4I_{15/2}$) appear at intermediate $Yb^{3+}$:$Er^{3+}$ ratios (2:1 and 1:2). The results highlight the role of $Yb^{3+}$ co-doping in facilitating $^4S_{3/2} \rightarrow {}^4I_{15/2}$ transition [47,48].

### 2.4. Considerations for $Yb^{3+}$:$Er^{3+}$ Co-doped $ZrO_2$ microarchitectures

The fabrication of $Yb^{3+}$:$Er^{3+}$ co-doped $ZrO_2$ microarchitectures through TPL and subsequent thermal treatment provides a pathway for investigating luminescence properties in structured ceramic systems. The results presented here show that dopant incorporation, phase evolution, and defect formation influence the emission response of these microarchitectures. The spectral characteristics analyzed through CL and PL highlight the role of processing conditions in shaping luminescence behavior, with CL exhibiting more consistent spectral features and PL showing greater variation, likely due to differences in excitation energy and penetration depth. The influence of thermal treatment is particularly relevant [49,50], as crystallite size evolution and the *t*-$ZrO_2$ to *m*-$ZrO_2$ phase modify the host environment of the lanthanide ions, which can, in turn, affect the observed emissions.

Although the luminescence response of $Yb^{3+}$ and $Er^{3+}$ in co-doped $ZrO_2$ systems has been widely studied in bulk materials [51], the specific impact of microstructure on these emissions requires further analysis. Defect-related emissions observed in early annealing cycles suggest that the presence of oxygen vacancies, carbon impurities, and variations in crystallinity play a role in the photoluminescence of the fabricated structures, similar to what has been reported in bulk $ZrO_2$ [52]. Nevertheless, the extent to which these defects influence emission pathways in printed microarchitectures remains an open question. As structural characterization indicates differences in crystallite size between printed and bulk materials, the possibility of changes in the local chemical environment of dopants should be considered, particularly during phase transformation at high temperatures [52].

To further understand the luminescence mechanisms observed in the codoped $Yb^{3+}$:$Er^{3+}$ microarchitectures, we propose a qualitative discussion of possible ET and CR pathways (**Support Information, Section 5**). The measured emission spectra indicate an enhancement in $Er^{3+}$ luminescence in codoped samples, particularly in the green and red spectral regions. The presence of $Yb^{3+}$ appears to facilitate additional ET processes, influencing the relative intensities of $Er^{3+}$ emissions.

We hypothesize that in $Er^{3+}$ single-doped microarchitectures, excitation at 325 nm primarily populates higher-energy $Er^{3+}$ states, which may undergo rapid CR processes, leading to non-radiative losses or direct interaction with the host matrix. In contrast, the presence of $Yb^{3+}$ may provide alternative ET routes that enhance $Er^{3+}$ emission by suppressing host-related defect states. As shown in **Figure S5**, we propose possible ET pathways, including ET1, which promotes the population of the $^4F_{9/2}$ state, thereby enhance red and infrared emission. Additional ET2 and ET3 pathways could favor the population of the $^4F_{7/2}$ and $^2H_{9/2}$ states, contributing to green emissions. These pathways may explain the observed changes in emission intensity ratios between green and red/infrared emissions at different $Yb^{3+}$ concentrations. However, these

interpretations remain qualitative, as a definitive identification of ET mechanisms requires additional experimental data, such as time-resolved spectroscopy or excitation-dependent measurements over such scale architectures. Further studies are necessary to estimate the lifetimes and ET efficiencies between $Yb^{3+}$ and $Er^{3+}$ in these 3D microarchitectures.

Future work can refine the understanding of how dopant incorporation and processing conditions impact the luminescence of these microarchitectures. Exploring different lanthanide dopants and their concentrations may provide insights into how emission properties evolve in structured ceramic systems. Advanced spectroscopic techniques, such as time-resolved photoluminescence, could offer a more detailed view of luminescence dynamics, while computational methods may aid in deconvoluting the structural effects on emission trends. These approaches would contribute to a broader understanding of dopant-host interactions in 3D-printed ceramic architectures while building upon the findings presented in this study.

## 3. Conclusions

This study examined the effects of thermal treatment on the luminescence properties of 3D $Yb^{3+}$ and $Er^{3+}$-doped *t*-$ZrO_2$ microarchitectures fabricated using TPL. We explored dopant ratios of $Yb^{3+}$:$Er^{3+}$ at 7:1, 2:1, 1:2, and 1:7 alongside single-doped systems (2.5 mol% and 0.35 mol% $Yb^{3+}$ or $Er^{3+}$) to evaluate the influence of concentration and thermal annealing on luminescence behavior. Thermal annealing at 600°C, 750°C, and 1000°C is conducted to assess phase transitions, crystallinity, and their impact on the photoemission. CL and PL measurements revealed distinct behaviors between single- and co-doped systems, with co-doped microarchitectures annealed at 1000 °C demonstrating superior luminescent properties. PL measurements of (co-)doped microarchitectures annealed at 1000 °C confirm $Yb^{3+}$ emissions ($^2F_{5/2} \rightarrow {}^2F_{7/2}$ at 975 nm) and $Er^{3+}$ emissions ($^4S_{3/2} \rightarrow {}^4I_{15/2}$ and $^4F_{9/2} \rightarrow {}^4I_{15/2}$). Although the 325 nm excitation does not directly target $Yb^{3+}$ absorption, the enhanced $Er^{3+}$ luminescence observed in co-doped microarchitectures is attributed to an indirect cooperative interaction—mediated by host matrix defects and ET between $Yb^{3+}$ and $Er^{3+}$—that promotes efficient $Er^{3+}$ emission. Notably, single-doped microarchitectures showed larger contributions from defects. From a broad perspective, this work highlights the compatibility of TPL for fabricating complex 3D luminescent ceramic microarchitectures with tunable optical properties, paving the way for applications in optics, like sensors [22].

## 4. Experimental Methods

### 4.1. Materials

All chemicals were used as received without further purification. Zirconium methacrylate (ZrM, 95%) was sourced from Gelest. Glacial acetic acid (≥99%), N,N-dimethylacetamide (DMAc, ≥99.8%, anhydrous), pentaerythritol triacrylate (PETA, technical grade) was sourced from Sigma-Aldrich. Diethyl-triamine pentaacetic acid ester (DETC, 97%) was acquired from abcr, while dichloromethane (DCM, ≥99.7%, anhydrous, stabilized with amylene) was provided by Alfa Aesar. Lanthanide precursors, including erbium(III) acetate tetrahydrate (99.9%) and ytterbium(III) acetate hydrate (99.9%), were supplied by Thermo Scientific Chemicals. HPLC-grade isopropanol (IPA) was purchased from Supelco.

### 4.2. Zirconium-rich photoresin

The zirconium-rich photoresin was prepared by dissolving zirconium methacrylate (ZrM, 86.5 mg, 0.2 mmol) in acetic acid (150 mg, 2.50 mmol), DMAc (500 mg, 5.7 mmol), and DCM (2000 mg, 23.6 mmol) in a pear-shaped glass flask (50 mL). The flask was connected to a rotary evaporator and rotated at 150 rpm in a 40°C water bath under ambient pressure for 1 hour. Pentaerythritol triacrylate (PETA, 300 mg, 1.01 mmol) was then added to the solution, followed by additional mixing for another hour. Finally, diethyl-triamine pentaacetic acid ester (DETC, 23 mg, 76.8 μmol) and an extra aliquot of DCM (100 mg, 1.18 mmol) were introduced and mixed at 40°C and rotated at 180 rpm under reduced pressure for 30 minutes. The homogeneity of the photoresin was verified by drop-casting a small amount onto a silicon substrate and examining it under an optical microscope equipped with a 100x/0.9 objective lens. Once confirmed to be homogeneous, the photoresin was used directly for fabrication. All steps were carried out under yellow light to avoid unintended photopolymerization.

### 4.3. Lanthanide-doped zirconium-rich photoresin

Eight different lanthanide-doped photoresins were prepared to study the emission properties of $Yb^{3+}$ and $Er^{3+}$ ions in $ZrO_2$ microarchitectures. These included four single-doped formulations (two each for $Yb^{3+}$ and $Er^{3+}$) and four co-doped formulations with varying Yb:Er molar ratios. Dopant concentrations were carefully chosen to avoid saturation of the resin while enabling detailed analysis of ET and luminescence properties.

For the single-doped photoresins, ytterbium(III) acetate hydrate ($YbAc \times H_2O$) and erbium(III) acetate tetrahydrate ($ErAc \times H_2O$) were added to the zirconium-rich photoresin at two concentrations each: $Yb^{3+}$ (2.5 mol%): 1.79 mg (5.11 μmol), $Yb^{3+}$ (0.35 mol%): 0.25 mg (0.70 μmol), $Er^{3+}$ (2.5 mol%): 1.72 mg (5.10 μmol, interpolated) and $Er^{3+}$ (0.35 mol%): 0.24 mg (0.70 μmol).

For the co-doped photoresins, Yb:Er molar ratios were adjusted with the following combinations and concentrations: 7:1 (2.5 mol% Yb, 0.35 mol% Er): 1.79 mg $YbAc \times H_2O$ (5.11 μmol) and 0.24 mg $ErAc \times H_2O$ (0.70 μmol), 2:1 (1.25 mol% Yb, 0.66 mol% Er): 0.90 mg $YbAc \times H_2O$ (2.56 μmol, interpolated) and 0.45 mg $ErAc \times H_2O$ (1.31 μmol, interpolated), 1:2 (0.66 mol% Yb, 1.25 mol% Er): 0.48 mg $YbAc \times H_2O$ (1.37 μmol, interpolated) and 0.86 mg $ErAc \times H_2O$ (2.50 μmol) and 1:7 (0.35 mol% Yb, 2.5 mol% Er): 0.25 mg $YbAc \times H_2O$ (0.70 μmol) and 1.72 mg $ErAc \times H_2O$ (5.10 μmol). Dopants were dissolved in the zirconium-rich photoresin following Section 4.2 to ensure homogeneous distribution.

### 4.4. TPL Manufacturing

Inorganic-organic 3D microarchitectures were fabricated using a commercial Nanoscribe Photonic Professional GT system. The fabrication setup consisted of a circular glass coverslip (170 μm thickness, 30 mm diameter) mounted on the sample holder with immersion oil (Immersol 518 F, Carl Zeiss) and fixed in place using rubber cement. A custom-made lanthanide-doped photoresin droplet was placed on the coverslip, confined between two parallel polyimide film tape ribbons (100 μm thickness, 12 mm length, 3 mm width). A 63 × /1.4 NA oil immersion objective (Plan-Apochromat, Carl Zeiss) was employed to focus the laser beam for TPL. In reflection mode, a 9 × 9 mm silicon substrate was used to cover the resin droplet and served as the printing surface for fabricating the 3D microarchitectures. The focal spot provided an optical lateral resolution of 278.6 nm and an axial resolution of 398 nm, ensuring precise feature definition. The laser power and exposure time were adjusted to achieve a two-photon polymerization dose of approximately 340 mJ/cm$^2$, sufficient for crosslinking the resin. Post-fabrication, the microarchitectures were developed in methanol (5 min) to remove unpolymerized resin, followed by a 1-minute IPA rinse for final cleaning. The microarchitectures were then left to air dry overnight at room temperature before being subjected to thermal annealing.

### 4.5. Pulverized UV-cured photoresin

To prepare pulverized photoresin for thermal analysis, the custom-

made lanthanide-doped photoresins were poured onto a glass petri dish, forming a thin film. The films were cured under a commercial 36 W halogen ultraviolet lamp (EBN001, Esperanza) for 6 hours to ensure complete polymerization of the resin. After curing, the solid organic-inorganic polymer film was carefully removed from the petri dish surface using a scraper. The extracted polymer was then manually pulverized into fine particles to facilitate uniform annealing in subsequent thermal treatments. The pulverized resin microarchitectures were stored in sealed containers to prevent contamination and used directly for thermal studies under the same conditions as the 3D microarchitectures.

### 4.6. Thermal Annealing Preparation

The TPL 3D-printed microarchitectures on silicon substrates and pulverized-cured photoresins were placed in a chamber furnace (LH 15/12, Nabertherm). An initial annealing cycle of a two-stage heating process in ambient air was carried out. A heating ramp of 1°C $min^{-1}$ was set until it reached 500°C, and the temperature was kept at that level for 1 hour. Then, the same ramp of 1°C $min^{-1}$ was applied until it reached a final temperature of 600°C maintained for 1 hour and left to cool down at room temperature. Afterward, a second annealing cycle was carried out, only modifying the final temperature to 750°C. In addition, the pulverized UV-cured resin powders were placed in crucibles, followed by the same annealing treatment of the microarchitectures. The TPL-fabricated 3D microarchitectures on silicon substrates and the pulverized UV-cured photoresin powders were subjected to a series of thermal annealing cycles to investigate the effects of temperature on crystallinity and luminescence. All annealing procedures were carried out in a chamber furnace (LH 15/12, Nabertherm) under an air atmosphere. The annealing process consisted of three cycles: Cycle 1: A heating ramp of 1°C $min^{-1}$ was applied until the temperature reached 500°C. The temperature was maintained at 500°C for 1 hour. The same ramp of 1°C $min^{-1}$ was continued to reach a final temperature of 600°C, which was held for 1 hour. The furnace was then allowed to cool naturally to room temperature. Cycle 2: The annealing procedure was repeated with the final temperature modified to 750°C, which was held for 1 hour. Cycle 3: A final heating cycle was done with the same ramp rate to a maximum temperature of 1000°C, which was held for 1 hour before cooling to room temperature.

### 4.7. Micro PL Spectroscopy

Micro-Raman and PL measurements were conducted at room temperature using a Horiba Jobin-Yvon LabRAM HR800 confocal microscope equipped with a Peltier-cooled CCD detector and a 600 l/mm grating. The system was equipped with a 40 × MicroSpot® focusing objective for high-resolution analysis and a He-Cd laser (λ = 325 nm, output power ~2 mW) as the excitation source, providing a spot size of approximately 1 μm in diameter.

### 4.8. CL Spectroscopy

Room-temperature CL measurements were performed using a JEOL JIB-4500 SEM equipped with a Gatan MonoCL4 system, containing a Hamamatsu photomultiplier tube (model R6249A). The measurements were conducted at an acceleration voltage of 15 kV to analyze the luminescence properties of the microarchitectures under electron beam excitation.

### 4.9. SEM and SEM-EDX

SEM was carried out to obtain top-view images of the 3D microarchitectures using a Carl Zeiss Merlin AURIGA CrossBeam Workstation. The system was equipped with Inlens and High-Efficiency Secondary Electron (HE-SE2) detectors to capture detailed surface morphology. Imaging was carried out at an acceleration voltage ranging from 1.5 to 2.2 kV, ensuring optimal resolution while minimizing sample charging effects. Elemental mapping was conducted using an EDX attachment integrated into the SEM system. This allowed for spatially resolved compositional analysis of the microarchitectures. The EDX data were processed and analyzed using AZtec software (Oxford Scientific) to confirm the distribution of lanthanide dopants ($Yb^{3+}$ and $Er^{3+}$) and other elements within the microarchitectures.

### 4.10. XRD measurements on powders

To analyze the crystalline phases of the annealed cured resin microarchitectures, the powdered materials were cast onto a zero-diffraction plate for characterization using a Bruker D2 Phaser diffractometer. The instrument operated at 30 kV and 10 mA and was equipped with a LynxEye detector. Cu-Kα radiation (λ = 1.5406 Å) was used as the X-ray source. XRD measurements were carried out over a 2θ range of 20°–80° at a scan speed of 2.25°/min.

### 4.11. FIB and TEM analysis

Cross-sectional lamellae of Yb-doped ZrO2 microarchitectures were prepared using a Helios 5 UX DualBeam workstation with Ga ion milling. Thinning and polishing were carried out with W and Si ions, and lamellae were mounted on Cu grids. TEM analysis was conducted using a Spectra 300 station (300 kV, 173 pA) and a JEOL ARM 200CF operated at 200 kV equipped with an SDD Jeol Centurio spectrometer.

## CRediT authorship contribution statement

**Cristian Rosero-Arias:** Writing – original draft, Validation, Methodology, Investigation, Formal analysis, Data curation, Conceptualization. **Geraldo Cristian Vásquez:** Writing – original draft, Methodology, Investigation, Funding acquisition, Formal analysis, Data curation. **Manuel Herrera-Zaldívar:** Writing – original draft, Validation, Methodology, Investigation, Funding acquisition, Formal analysis. **R. Margoth Córdova-Castro:** Writing – original draft, Visualization, Validation, Methodology, Investigation, Formal analysis. **Israel De Leon:** Writing – original draft, Supervision. **Francisco Ruiz-Zepeda:** Validation, Investigation, Formal analysis, Data curation. **Han Gardeniers:** Writing – review & editing, Writing – original draft, Validation, Supervision, Resources, Project administration. **David Maestre:** Writing – review & editing, Writing – original draft, Supervision, Funding acquisition. **Alan Aguirre-Soto:** Writing – review & editing, Writing – original draft, Supervision, Funding acquisition. **Arturo Susarrey-Arce:** Writing – review & editing, Writing – original draft, Supervision, Project administration.

## Declaration of competing interest

We wish to confirm that there are no known conflicts of interest associated with this publication, and there has been no significant financial support for this work that could have influenced its outcome.

## Acknowledgments

The authors thank Mark Smithers for acquiring high-resolution SEM images and Dr. Melissa Goodwin's assistance during the FIB milling. The microarchitectures were manufactured at the MESA+ Institute for Nanotechnology, and the materials were analyzed at the MESA+ Institute for Nanotechnology of the University of Twente. C.R.A. received funding from Mexico CONAHCYT (Grant No. 1061739). GCV, DM, and MHZ acknowledge funding from projects PID2021-122562NB-I00PID, MAD2D-CM-UCM4, and IN104724. F.R-Z. would like to thank the Slovenian research agency (ARRS) program P2–0393.

## Supplementary materials

Supplementary material associated with this article can be found, in the online version, at doi:10.1016/j.apmt.2025.102714.

## Data availability

Data will be made available on request.

## References


[1] A. Tiwari, P.K. Iyer, V. Kumar, H. Swart (Eds.), Advanced Magnetic and Optical Materials, Wiley, 2016, https://doi.org/10.1002/9781119241966.

[2] J.-C.G. Bünzli, C. Piguet, Taking advantage of luminescent lanthanide ions, Chem Soc Rev 34 (2005) 1048, https://doi.org/10.1039/b406082m.

[3] K.Lingeshwar Reddy, R. Balaji, A. Kumar, V. Krishnan, Lanthanide Doped Near Infrared Active Upconversion Nanophosphors: Fundamental Concepts, Synthesis Strategies, and Technological Applications, Small 14 (2018) 1801304, https://doi.org/10.1002/smll.201801304.

[4] C. Willa, A. Schmid, D. Briand, J. Yuan, D. Koziej, Lightweight, Room-Temperature CO2 Gas Sensor Based on Rare-Earth Metal-Free Composites—An Impedance Study, ACS Appl Mater Interfaces 9 (2017) 25553–25558, https://doi.org/10.1021/acsami.7b07379.

[5] A.K.R. Junker, M. Tropiano, S. Faulkner, T.J. Sørensen, Kinetically Inert Lanthanide Complexes as Reporter Groups for Binding of Potassium by 18-crown-6, Inorg Chem 55 (2016) 12299–12308, https://doi.org/10.1021/acs.inorgchem.6b02063.

[6] H.S. Lokesha, M.L. Chithambo, S. Chikwembani, Thermoluminescence of monoclinic ZrO2: Kinetic analysis and dosimetric features, J Lumin 218 (2020) 116864, https://doi.org/10.1016/j.jlumin.2019.116864.

[7] X. Zhao, D. Vanderbilt, Phonons and lattice dielectric properties of zirconia, Phys Rev B 65 (2002) 075105, https://doi.org/10.1103/PhysRevB.65.075105.

[8] J. Winczewski, J. Arriaga-Dávila, D. Maestre, M. Herrera-Zaldívar, H. Gardeniers, A. Susarrey-Arce, Additive Manufacturing of Zn-Doped ZrO2 Architectures, Adv Eng Mater 26 (2024) 2400187, https://doi.org/10.1002/ADEM.202400187.

[9] S. Shukla, S. Seal, R. Vij, S. Bandyopadhyay, Z. Rahman, Effect of Nanocrystallite Morphology on the Metastable Tetragonal Phase Stabilization in Zirconia, Nano Lett 2 (2002) 989–993, https://doi.org/10.1021/nl025660b.

[10] A.G. Bispo-Jr, A.J. de Morais, C.M.S. Calado, I.O. Mazali, F.A. Sigoli, Lanthanide-doped luminescent perovskites: A review of synthesis, properties, and applications, J Lumin 252 (2022) 119406, https://doi.org/10.1016/j.jlumin.2022.119406.

[11] J.P. Winczewski, J. Arriaga-Dávila, C. Rosero-Arias, A. Susarrey-Arce, Tailoring chemistry for inorganic 3D micro-optics, Trends Chem 6 (2024) 58–61, https://doi.org/10.1016/j.trechm.2023.12.005.

[12] B. Bawanthade, A. Mistry, N. Ugemuge, S.J. Dhoble, Synthesis and study of structure and optical properties of RE3+(RE = Sm3+ and Tb3+) activated Ca8NaBi(PO4)6F2 orange-red and green emitting phosphors prepared by Pechini method, Journal of Materials Science: Materials in Electronics 35 (2024) 355, https://doi.org/10.1007/s10854-024-12093-7.

[13] J. Zhou, G. Zheng, X. Liu, G. Dong, J. Qiu, Defect engineering in lanthanide doped luminescent materials, Coord Chem Rev 448 (2021) 214178, https://doi.org/10.1016/J.CCR.2021.214178.

[14] H. Chu, M. Xu, B. Liu, Z. Pan, H. Pan, S. Zhao, D. Xu, D. Li, Fabrication of amorphous nanoporous ZrO2/SiO2 aerogel enabling nonlinear optical properties, Journal of Materiomics 10 (2024) 1109–1116, https://doi.org/10.1016/j.jmat.2023.11.014.

[15] T. Li, Y. Huang, J.X.M. Chen, Y.-C. Sun, O. Aghababaei, Z. Saadatnia, H.E. Naguib, 3D printing of conductive polymer aerogel thermoelectric generator with tertiary doping, Nano Energy 117 (2023) 108909, https://doi.org/10.1016/j.nanoen.2023.108909.

[16] D. Navas, S. Fuentes, A. Castro-Alvarez, E. Chavez-Angel, Review on Sol-Gel Synthesis of Perovskite and Oxide Nanomaterials, Gels 7 (2021) 275, https://doi.org/10.3390/gels7040275.

[17] C. Rosero-Arias, G.C. Vásquez, N.G. Davila-Montero, J. Winczewski, B. Mei, I. De Leon, D. Maestre, H. Gardeniers, A. Aguirre-Soto, A. Susarrey-Arce, Temperature Promotes Photoluminescence in Lanthanide-Doped 3D Ceramic Microarchitectures, Adv Mater Interfaces 11 (2024) 2400339, https://doi.org/10.1002/admi.202400339.

[18] F. Jobin, P. Paradis, Y.O. Aydin, T. Boilard, V. Fortin, J.-C. Gauthier, M. Lemieux-Tanguay, S. Magnan-Saucier, L.-C. Michaud, S. Mondor, L.-P. Pleau, L. Talbot, M. Bernier, R. Vallée, Recent developments in lanthanide-doped mid-infrared fluoride fiber lasers, Opt Express 30 (2022) 8615, https://doi.org/10.1364/OE.450929.

[19] J.P. Winczewski, J. Arriaga Dávila, M. Herrera-Zaldívar, F. Ruiz-Zepeda, R. M. Córdova-Castro, C.R. Pérez de la Vega, C. Cabriel, I. Izeddin, H. Gardeniers, A. Susarrey-Arce, 3D-Architected Alkaline-Earth Perovskites, Advanced Materials 36 (2024) 2307077, https://doi.org/10.1002/adma.202307077.

[20] J. Fan, L. Zhang, S. Wei, Z. Zhang, S.-K. Choi, B. Song, Y. Shi, A review of additive manufacturing of metamaterials and developing trends, Materials Today 50 (2021) 303–328, https://doi.org/10.1016/j.mattod.2021.04.019.

[21] G. Merkininkaite, D. Gailevicius, L. Staisiunas, E. Ezerskyte, R. Vargalis, M. Malinauskas, S. Sakirzanovas, Additive Manufacturing of SiOC, SiC, and $Si_3N_4$ Ceramic 3D Microstructures, Adv Eng Mater 25 (2023) 2300639, https://doi.org/10.1002/adem.202300639.

[22] J. Arriaga-Dávila, C. Rosero-Arias, D. Jonker, M. Córdova-Castro, J. Zscheile, R. Kirchner, A. Aguirre-Soto, R. Boyd, I. De Leon, H. Gardeniers, A. Susarrey-Arce, From Single to Multi-Material 3D Printing of Glass-Ceramics for Micro-Optics, Small Methods (2025), https://doi.org/10.1002/smtd.202401809.

[23] J. Winczewski, M. Herrera, C. Cabriel, I. Izeddin, S. Gabel, B. Merle, A. Susarrey Arce, H. Gardeniers, Additive Manufacturing of 3D Luminescent $ZrO_2$:$Eu^{3+}$ Architectures, Adv Opt Mater 10 (2022) 2102758, https://doi.org/10.1002/adom.202102758.

[24] A. Desponds, A. Banyasz, D. Chateau, A. Tellal, A. Venier, S. Meille, G. Montagnac, J. Chevalier, C. Andraud, P.L. Baldeck, S. Parola, 3D Printing and Pyrolysis of Optical $ZrO_2$ Nanostructures by Two-Photon Lithography: Reduced Shrinkage and Crystallization Mediated by Nanoparticles Seeds, Small 17 (2021) 2102486, https://doi.org/10.1002/smll.202102486.

[25] J.P. Winczewski, S. Zeiler, S. Gabel, A. Susarrey-Arce, J.G.E. Gardeniers, B. Merle, Exploring the mechanical properties of additively manufactured carbon-rich zirconia 3D microarchitectures, Mater Des 232 (2023) 112142, https://doi.org/10.1016/j.matdes.2023.112142.

[26] J. Winczewski, M. Herrera, H. Gardeniers, A. Susarrey-Arce, White emission in 3D-printed phosphor microstructures, Chemical Communications 59 (2023) 3095–3098, https://doi.org/10.1039/D2CC06953A.

[27] H.S. Lokesha, N. Chauhan, K.R. Nagabhushana, F. Singh, Dosimetric properties of ZrO2 and ZrO2:Sm3+ exposed to beta rays, Ceram Int 44 (2018) 18871–18877, https://doi.org/10.1016/j.ceramint.2018.07.122.

[28] G. Torres Jasso, E. Montes, J.C. Guzmán Olguín, D. Sánchez Guzmán, R.I. López Esquivel, I.R. Martín, J. Guzmán Mendoza, Upconversion emission of ZrO2 nanoparticles doped with erbium (Er3+) and ytterbium (Yb3+), synthesized by hydrothermal route, Ceram Int 44 (2018) 154–157, https://doi.org/10.1016/J.CERAMINT.2017.09.152.

[29] W.S. Yoo, B.G. Kim, S.W. Jin, T. Ishigaki, K. Kang, Ultra-Thin SiO2/Si Interface Quality In-Line Monitoring Using Multiwavelength Room Temperature Photoluminescence and Raman Spectroscopy, ECS Journal of Solid State Science and Technology 3 (2014) N142–N150, https://doi.org/10.1149/2.0181411jss.

[30] H.K. Yueh, B. Cox, Luminescence properties of zirconium oxide films, Journal of Nuclear Materials 323 (2003) 57–67, https://doi.org/10.1016/j.jnucmat.2003.08.025.

[31] M. Thakur, A. Vij, F. Singh, V.S. Rangra, Spectroscopic studies of metastable tetragonal ZrO2 nanocrystals, Spectrochim Acta A Mol Biomol Spectrosc 305 (2024) 123495, https://doi.org/10.1016/j.saa.2023.123495.

[32] A. Chen, Y. Zhou, S. Miao, Y. Li, W. Shen, Assembly of monoclinic ZrO2 nanorods: formation mechanism and crystal phase control, CrystEngComm 18 (2016) 580–587, https://doi.org/10.1039/C5CE02269J.

[33] Y. Zhang, H.-X. Chen, L. Duan, J.-B. Fan, L. Ni, V. Ji, A comparison study of the structural and mechanical properties of cubic, tetragonal, monoclinic, and three orthorhombic phases of ZrO2, J Alloys Compd 749 (2018) 283–292, https://doi.org/10.1016/j.jallcom.2018.03.253.

[34] M.F. Bekheet, L. Schlicker, R. Popescu, W. Riedel, M. Grünbacher, S. Penner, A. Gurlo, A quantitative microscopic view on the gas-phase-dependent phase transformation from tetragonal to monoclinic ZrO2, Journal of the American Ceramic Society 107 (2024) 5036–5050, https://doi.org/10.1111/jace.19749.

[35] J. Málek, L. Beneš, T. Mitsuhashi, Powder diffraction data and Rietveld refinement of metastable t-ZrO2 at low temperature, Powder Diffr 12 (1997) 96–98, https://doi.org/10.1017/S0885715600009519.

[36] V. Dorcet, P. Marchet, J.P. Mercurio, Dielectric Properties of Na 0.5 Bi 0.5 TiO3-PbZrO3 Ceramics, Ferroelectrics 339 (2006) 29–35, https://doi.org/10.1080/00150190600737909.

[37] A.S. Ivanov, V.I. Vasilev, I.V. Sedova, S.V. Sorokin, A.A. Sitnikova, S.G. Konnikov, T.B. Popova, M.V. Zamoryanskaya, Cathodoluminescence of laser AIIBVI heterostructures, Semiconductors 41 (2007) 478–481, https://doi.org/10.1134/S1063782607040239.

[38] M. Boffelli, W. Zhu, M. Back, G. Sponchia, T. Francese, P. Riello, A. Benedetti, G. Pezzotti, Oxygen Hole States in Zirconia Lattices: Quantitative Aspects of Their Cathodoluminescence Emission, J Phys Chem A 118 (2014) 9828–9836, https://doi.org/10.1021/jp506923p.

[39] C. Lin, C. Zhang, J. Lin, Phase Transformation and Photoluminescence Properties of Nanocrystalline $ZrO_2$ Powders Prepared via the Pechini-type Sol−Gel Process, The Journal of Physical Chemistry C 111 (2007) 3300–3307, https://doi.org/10.1021/jp066615l.

[40] X. Wang, X. Tan, S. Xu, F. Liu, B.A. Goodman, W. Deng, Preparation and up-conversion luminescence of Er-doped yttria stabilized zirconia single crystals, J Lumin 219 (2020) 116896, https://doi.org/10.1016/j.jlumin.2019.116896.

[41] B. Huang, J. Bergstrand, S. Duan, Q. Zhan, J. Widengren, H. Ågren, H. Liu, Overtone Vibrational Transition-Induced Lanthanide Excited-State Quenching in $Yb^{3+}$/$Er^{3+}$ -Doped Upconversion Nanocrystals, ACS Nano 12 (2018) 10572–10575, https://doi.org/10.1021/acsnano.8b05095.

[42] L. Aarts, B.M. van der Ende, A. Meijerink, Downconversion for solar cells in NaYF4: Er,Yb, J Appl Phys 106 (2009), https://doi.org/10.1063/1.3177257.

[43] P. Babu, I.R. Martín, V. Lavín, U.R. Rodríguez-Mendoza, H.J. Seo, K. V. Krishanaiah, V. Venkatramu, Quantum cutting and near-infrared emissions in Ho3+/Yb3+ codoped transparent glass-ceramics, J Lumin 226 (2020) 117424, https://doi.org/10.1016/j.jlumin.2020.117424.

[44] F.T. Aquino, J.L. Ferrari, S.J.L. Ribeiro, A. Ferrier, P. Goldner, R.R. Gonçalves, Broadband NIR emission in novel sol–gel Er3+-doped SiO2–Nb2O5 glass ceramic planar waveguides for photonic applications, Opt Mater (Amst) 35 (2013) 387–396, https://doi.org/10.1016/j.optmat.2012.09.029.

[45] J. Méndez-Ramos, V.K. Tikhomirov, V.D. Rodríguez, D. Furniss, Infrared tuneable up-conversion phosphor based on Er3+-doped nano-glass–ceramics, J Alloys Compd 440 (2007) 328–332, https://doi.org/10.1016/j.jallcom.2006.09.033.
[46] D. Avram, I. Tiseanu, B.S. Vasile, M. Florea, C. Tiseanu, Near infrared emission properties of Er doped cubic sesquioxides in the second/third biological windows, Sci Rep 8 (2018) 18033, https://doi.org/10.1038/s41598-018-36639-y.
[47] H. Suo, X. Zhao, Z. Zhang, T. Li, E.M. Goldys, C. Guo, Constructing multiform morphologies of YF: Er3+/Yb3+ up-conversion nano/micro-crystals towards sub-tissue thermometry, Chemical Engineering Journal 313 (2017) 65–73, https://doi.org/10.1016/j.cej.2016.12.064.
[48] M. Li, L. Su, X. Chen, Q. Wu, B. Zhang, Effect of Yb3+ concentration on Er3+ doped CaF2 single crystal for temperature sensor applications, Opt Commun 520 (2022) 128488, https://doi.org/10.1016/j.optcom.2022.128488.
[49] W. Zheng, B. Sun, Y. Li, R. Wang, T. Lei, Y. Xu, Near-Infrared Laser-Triggered Full-Color Tuning Photon Upconversion and Intense White Emission in Single Gd2 O3 Microparticle, ACS Sustain Chem Eng 8 (2020) 2557–2567, https://doi.org/10.1021/acssuschemeng.9b07464.
[50] R. Anjana, P.P. Subha, M.K. Kurias, M.K. Jayaraj, Enhanced green upconversion luminescence in ZnO:Er3+, Yb3+ on Mo6+ co-doping for temperature sensor application, Methods Appl Fluoresc 6 (2017) 015005, https://doi.org/10.1088/2050-6120/aa9c13.
[51] C.S. Lim, Cyclic MAM synthesis and upconversion photoluminescence properties of CaMoO4:Er3+/Yb3+ particles, Mater Res Bull 47 (2012) 4220–4225, https://doi.org/10.1016/j.materresbull.2012.09.029.
[52] Q. Qiang, Y. Wang, Effect of Mn2+ on Upconversion Emission, Thermal Sensing and Optical Heater Behavior of Yb3+ - Er3+ Codoped NaGdF4 Nanophosphors, Front Chem 7 (2019), https://doi.org/10.3389/fchem.2019.00425.